

Critical fluctuations and noise spectra in two-dimensional Fe_3GeTe_2 magnets

Received: 23 September 2024

Accepted: 22 August 2025

Published online: 29 September 2025

 Check for updates

Yuxin Li^{1,2,3,4,9}, Zhe Ding^{1,2,4,9}, Chen Wang^{3,4,5,9}, Haoyu Sun^{1,2},
Zhousheng Chen^{1,2}, Pengfei Wang^{1,2,3,4}, Ya Wang^{1,2,3,4}, Ming Gong^{3,6}✉,
Hualing Zeng^{3,4,5}✉, Fazhan Shi^{1,2,3,4,7}✉ & Jiangfeng Du^{1,2,3,8}

Critical fluctuations play a crucial role in determining spin orders in low-dimensional magnetic materials. However, experimentally linking these fluctuations to scaling theory—and thereby uncovering insights into spin interaction models—remains a challenge. Here, we utilize a nitrogen-vacancy center-based quantum decoherence imaging technique to probe critical fluctuations in the van der Waals magnet Fe_3GeTe_2 . Our data reveal that critical fluctuations produce a random magnetic field, with noise spectra undergoing significant changes near the critical temperature. To explain this phenomenon, we developed a theoretical framework showing that the spectral density exhibits $1/f$ noise characteristics near the critical temperature, transitioning to white noise behavior away from this regime. By experimentally adjusting the sample-to-diamond distance, we identified the crossover temperature between these two noise types. These findings offer an approach to studying phase transition dynamics through critical fluctuations, enabling precise determination of critical exponents associated with long-range correlations. This methodology holds promise for advancing our understanding of critical phenomena across diverse physical systems.

Phase transitions and associated critical phenomena near thermodynamic critical points are fundamental research themes in modern condensed matter physics^{1–3}. Pioneering studies since the 1960s^{4–6} established that phase transitions are governed by divergent correlation lengths and emergent scale invariance, resulting in critical phenomena characterized by power-law singularities in thermodynamic quantities. These singularities manifest as distinctive scaling behaviors in macroscopic quantities such as magnetization, susceptibility, and specific heat. Their critical exponents, classified through the universality principle, form the cornerstone of critical

phenomena characterization⁷. Experimentally, critical exponents are typically determined by fitting the divergent behaviors of these quantities^{8–11}. Scaling laws establish fundamental relationships between critical exponents, demonstrating that singularities in macroscopic quantities originate from microscopic long-range correlations. While critical exponents associated with correlation length and time provide more direct insights into critical dynamics, their experimental determination remains challenging due to the simultaneous requirements of spatial and temporal resolution. Consequently, experimental characterization of phase transitions

¹CAS Key Laboratory of Microscale Magnetic Resonance and School of Physical Sciences, University of Science and Technology of China, Hefei 230026, China. ²Anhui Province Key Laboratory of Scientific Instrument Development and Application, University of Science and Technology of China, Hefei 230026, China. ³Hefei National Laboratory, University of Science and Technology of China, Hefei 230088, China. ⁴Hefei National Research Center for Physical Sciences at the Microscale, University of Science and Technology of China, Hefei 230026, China. ⁵International Center for Quantum Design of Functional Materials, University of Science and Technology of China, Hefei 230026, China. ⁶CAS Key Laboratory of Quantum Information, University of Science and Technology of China, Hefei 230026, China. ⁷School of Biomedical Engineering and Suzhou Institute for Advanced Research, University of Science and Technology of China, Suzhou 215123, China. ⁸Institute of Quantum Sensing and School of Physics, Zhejiang University, Hangzhou 310027, China. ⁹These authors contributed equally: Yuxin Li, Zhe Ding, Chen Wang. ✉e-mail: gongm@ustc.edu.cn; hlzeng@ustc.edu.cn; fzshi@ustc.edu.cn

has historically lacked a perspective rooted in these intrinsic parameters.

In magnetic systems, the extensively studied paramagnetic-ferromagnetic phase transition serves as a vital platform for investigating critical behaviors. The magnetic noise generated by thermally driven spin (cluster) fluctuations during phase transitions encodes information about long-range correlations^{12–14}. Consider an experiment where a sensor placed above a magnetic material measures magnetic perturbations caused by these fluctuations. This naturally raises two questions: (1) what quantities can be extracted from these measurements, and (2) how they reflect the critical physics. The power spectral density $S_B(\omega)$ of the measured magnetic field noise is directly related to the spectral density of magnetization $S_M(\omega)$. Crucially, as shown in ref. 15, the noise spectra exhibit a strong dependence on the reduced temperature $(T - T_c)/T_c$, where T_c is the critical temperature. Thus, noise spectrum measurements could provide essential insights into critical phenomena, including long-range correlations and critical exponents^{15–17}.

The nitrogen-vacancy (NV) centers^{18–20} in diamond are ideal quantum sensors for this purpose. Here, we employ NV centers to measure critical spin fluctuations in the van der Waals magnet Fe_3GeTe_2 , yielding two key findings. First, the NV centers' decoherence rate shows a pronounced peak at T_c , accompanied by a change in its temperature dependence. Second, we derive a theoretical model that quantitatively links the decoherence rate to both the noise spectra and the sensor-sample separation distance. Importantly, our experiments explicitly reveal the crossover from white noise to $1/f$ noise as the system approaches criticality. These results establish a framework for probing phase transitions through critical fluctuations across diverse quantum materials.

Results

We investigate the critical fluctuations in Fe_3GeTe_2 (hereafter abbreviated as FGT), a van der Waals magnet exhibiting a paramagnetic-ferromagnetic phase transition. FGT is an exfoliable magnet that retains robust ferromagnetism with strong out-of-plane anisotropy even at the monolayer limit^{9,21,22}. For bulk FGT, the T_c is approximately 210 K^{8,23}. When thinned down to a monolayer, T_c is significantly suppressed due to enhanced fluctuations²⁴, accompanied by a transition in magnetic properties from 3D to 2D Ising ferromagnetism^{22,23,25,26}.

The investigation of critical fluctuations near the critical point constitutes the primary focus of this work. To achieve this, we developed a cryogenic wide-field microscopy system utilizing ensemble NV centers²⁷, with the experimental configuration depicted in Fig. 1a. The system employs a linearly polarized 532 nm laser to initialize and read out the state of NV centers, while microwave radiation delivered through an antenna enables quantum state manipulation. An in-plane magnetic field was applied to lift the degeneracy of the $|\pm 1\rangle$ of NV centers and to avoid perturbing the intrinsic anisotropy of the FGT sample. Hexagonal boron nitride (hBN) substrates were transferred above and below the FGT flakes to prevent oxidation and to adjust the distance d between the FGT and NV centers, respectively. More details about the setup are presented in Supplementary Section 1.

NV centers, serving as quantum sensors, have become indispensable tools in condensed matter physics, materials science, and quantum sensing^{28–31}. The optically detected magnetic resonance technique enables static magnetic field sensing through continuous wave (CW) spectroscopy³², and dynamic decoupling protocols^{33–36} establish frequency domain detection channels, particularly effective for resolving varying magnetic signals through spectral engineering^{37,38}.

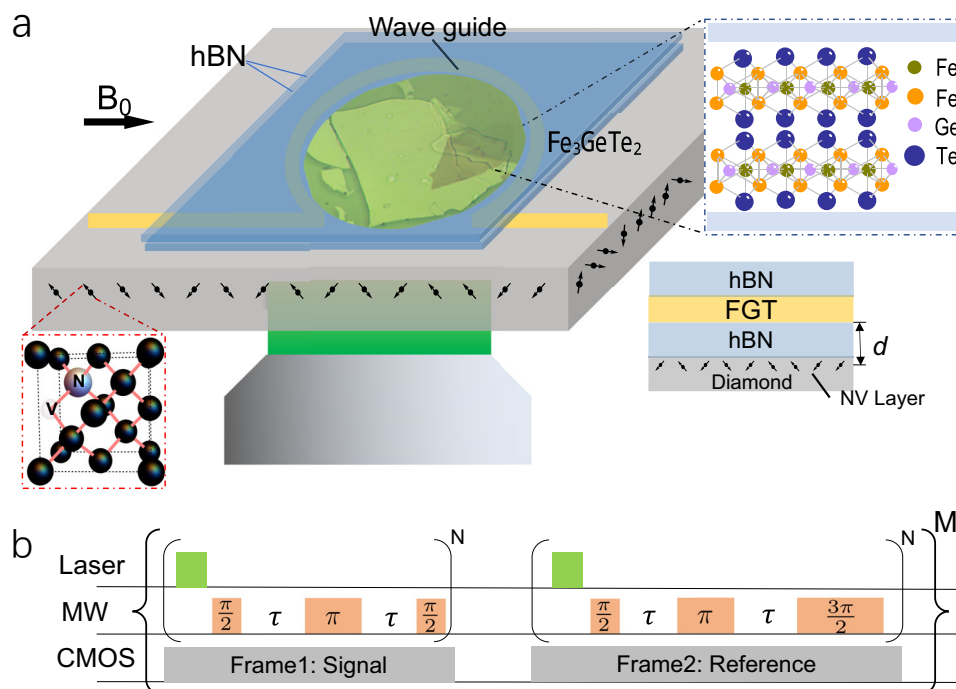


Fig. 1 | Experiment setup and pulse sequences. **a** Exfoliated FGT flakes are transferred to a [100] oriented diamond chip with single-layer ensemble NV centers. Black arrows in the diamond chip indicate the four possible orientations of the NV centers. Microwaves are radiated through an Ω -shaped wave guide, and the magnetic field B_0 is applied in-plane. hBN substrate layers are placed above and below the FGT flakes. Inset: Crystal structure of FGT and NV centers, where d denotes the NV-FGT distance. The crystal data were obtained at SpringerMaterials⁵⁹. **b** Hahn-echo pulse sequences for wide-field coherence

detection. Laser pulse initializes the state of NV centers to $|0\rangle$ and reads out the final state. The first $\pi/2$ microwave pulse drives the system to a superposition state. After free evolution for time τ , a π -pulse decouples noise components with frequencies beyond the $1/2\tau$ band. Final $\pi/2$ or $3\pi/2$ pulses convert coherence to $|0\rangle$ or $|1\rangle$ populations. A CMOS camera records photoluminescence from these populations as signal and reference frames, respectively. Each subsequence executes N times per frame. The pulse sequence is averaged over M 100–200 times for each τ .

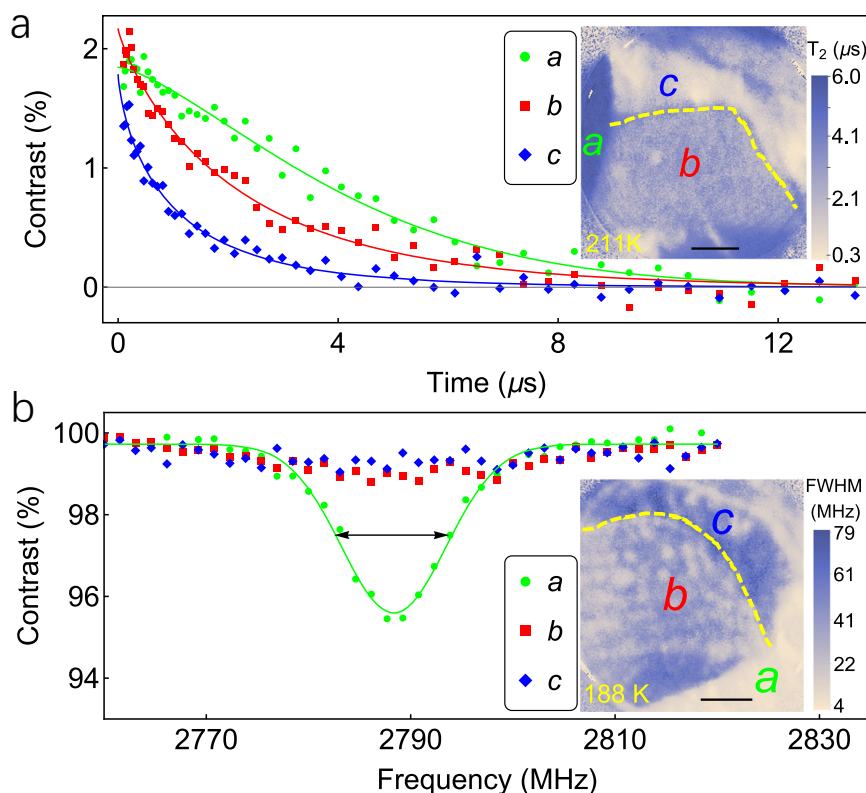


Fig. 2 | Dynamic and static magnetometry in paramagnetic and ferromagnetic states. **a** Decoherence curves of NV centers when FGT is in the paramagnetic phase. Solid lines represent fits using Eq. (1), yielding stretch exponents $\alpha = 1.306 \pm 0.113$ (green point), 0.772 ± 0.089 (red square), 0.698 ± 0.098 (blue rhombus). The inset shows the T_2 spatial map at 211 K. The colors of the lettered markers in each region

correspond to those of the decoherence curves. Statistical distributions of α and T_2 are provided in Supplementary Section 6. **b** CW spectrum of NV centers when FGT is in the ferromagnetic phase. The inset shows the FWHM map of the CW spectrum at 188 K. The data in both figures are measured from sample #6. Scale bar: 5 μm.

Notably, these methodologies have unveiled critical fluctuations in van der Waals magnets, including Fe_3GeTe_2 ³⁹, $\text{MnBi}_2\text{Te}_4(\text{Bi}_2\text{Te}_3)_n$ ⁴⁰, CrPS_4 ⁴¹, CrSBr ⁴², and twisted double trilayer CrI_3 ⁴³, primarily through relaxometry near phase transitions. The relaxation time of NV centers is predominantly governed by noise components at frequencies resonant with their energy levels, typically centered around 2.87 GHz. The observed increase in relaxation rate reflects enhanced spin fluctuations near the T_c . Meanwhile, subHertz magnetic domains' reverse has been observed in our previous work near the T_c ⁴⁴. These results demonstrate NV centers' capability to detect spin fluctuations across different time scales. Notably, the aforementioned works and ref. 45 have merely reported the existence of critical fluctuations, without exploring their underlying mechanisms, particularly failing to establish connections with scaling theory.

In contrast to previous experiments, our work leverages the quantum coherence of NV centers to probe critical fluctuations. The details of the NV centers and FGT samples are presented in Supplementary Sections 2 and 3. The Hahn-echo pulse sequence (Fig. 1b) exhibits a narrow-band spectral weight function, selectively coupling to noise components whose frequencies match the pulse sequence periodicity⁴⁶. This frequency-selective coupling modulates the coherence time of NV centers, enabling spectral mapping of magnetic fluctuations.

Multi-mode Imaging for static and fluctuating magnetic fields

Firstly, we perform wide-field imaging measurements to characterize the coherence time of NV centers adjacent to the FGT sample. When $T > T_c$, although the FGT is paramagnetic and lacks long-range magnetic order, local magnetic fluctuations still

suppress the coherence of NV centers. The results are presented in Fig. 2a. The decoherence of NV centers was measured through Hahn-echo pulse sequences, as shown in Fig. 1b. The contrast is defined as the normalized difference between the two frames: $C = (I_{\text{sig}} - I_{\text{ref}})/I_{\text{ref}}$, where I_{sig} (I_{ref}) is the gray value of the signal (reference) frame. The decoherence curves are depicted in Fig. 1a, which are obtained by recording contrast as a function of the pulse interval τ . By fitting the decoherence profile using

$$C(t) = C_0 \exp(-\chi(t)) = C_0 \exp(-(t/T_2)^\alpha), \quad (1)$$

where C_0 is a fitting parameter related to contrast; T_2 is the coherence time, determined by $\chi(t) = 1$; and α is the stretch exponent related to the properties of noise. The spatial variation of T_2 is presented in the inset. The sample comprises three regions. Region 'a': without FGT flakes and exhibiting the longest T_2 ; Region 'b': with a 70 nm-thick FGT flake and exhibiting intermediate T_2 ; Region 'c': with a 90 nm-thick FGT sample and exhibiting the shortest T_2 . The three curves in Fig. 2a demonstrate that magnetic noise originating from the FGT affects both the T_2 and the stretch exponent α . In region 'a', we observe $\alpha \approx 1.5$, consistent with previous reports in ref. 47. This value decreases significantly in FGT-covered regions 'b' and 'c'. The stretch exponent α is a rather subtle issue, which is affected by the inhomogeneity of the sample⁴⁷⁻⁴⁹.

In Fig. 2b, with $T < T_c$, spontaneous magnetization emerges in the FGT sample. We employ CW spectroscopy (see Supplementary Section 4) to map the static magnetic field distribution. A clear spectral dip at about 2.79 GHz is observed in region 'a', while in regions 'b' and 'c' the stray magnetic field from the FGT broadens the spectral lines and

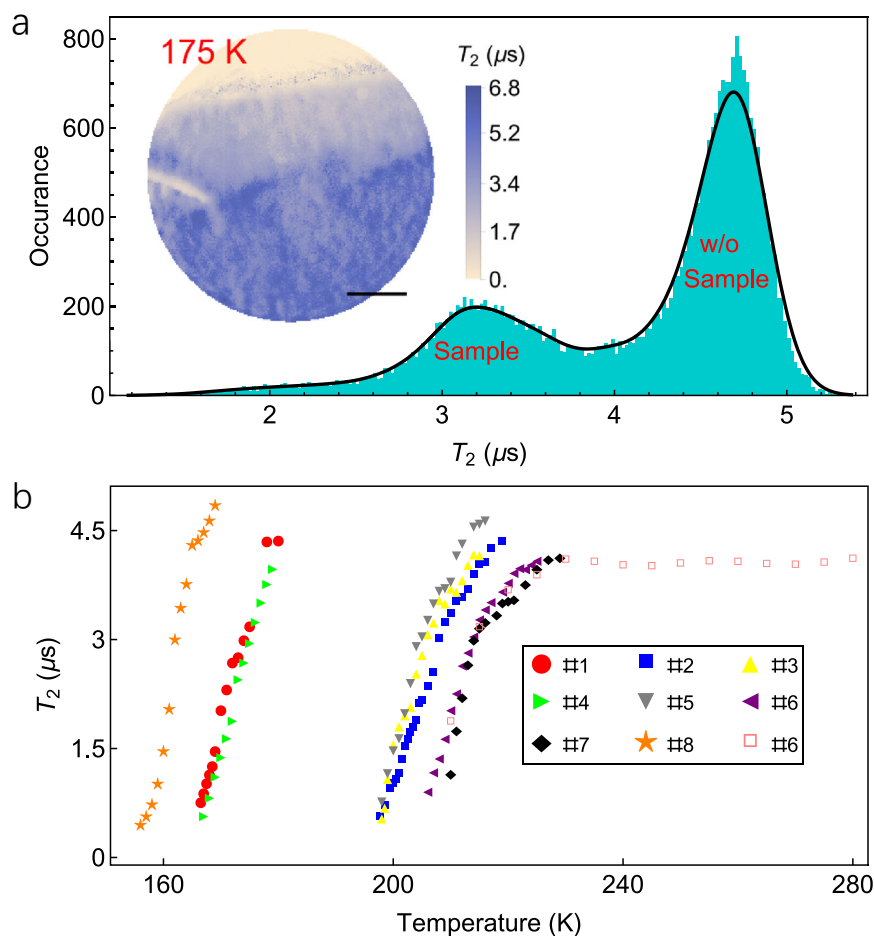


Fig. 3 | Distribution of T_2 and its temperature dependence. **a** Statistical distribution of T_2 across the field of view, measured from Sample #1 at 175 K. The two peaks in the histogram correspond to pixels inside and outside the FGT sample, respectively. The inset shows the corresponding T_2 map. The distribution of α is presented in Supplementary Section 6. **b** Temperature-dependent T_2 measured

from eight FGT samples (Sample #1–#8) above T_c . Data points with $T_2 \leq 500$ ns are excluded due to insufficient fitting reliability. By adjusting the NV-FGT distance, this can be resolved and Fig. 4b shows the complete measurement across T_c . On sample #6, two independent measurements were performed. Data marked with empty squares highlight that T_2 is unaffected when far from T_c . Scale bar: 5 μm .

reduces the contrast. In Supplementary Section 5, static magnetic field imaging of Sample #9 was performed at a temperature far below T_c , revealing distinct CW spectral characteristics between domain walls and interiors. Near domain walls, spectral lines are significantly broadened with nearly undetectable optical contrast, while in domain interiors, spectral lines maintain their intrinsic width. As shown in the inset of Fig. 2b, the spectral broadening observed across region 'b' originates from reduced magnetic domain sizes near T_c . Quasi-static noise arising from domain reversion may also contribute to this contrast reduction.

Huge critical magnetic fluctuations near the T_c

Next, we investigate the coherence dynamics of NV centers near the critical regime of FGT. As shown in Fig. 3a, the T_2 distribution exhibits two dominant peaks: a shorter value of approximately 3.2 μs in regions covered by FGT films and a longer value of 4.7 μs in FGT-free regions. We define the distribution peak position as the characteristic T_2 with the FGT sample. Further analysis in Fig. 3b represents the characteristic T_2 as a function of temperature for various samples with thicknesses ranging from 10 to 90 nm. All measured T_2 decreases monotonically as temperature approaches T_c from above. Although T_c varies with thickness (see Supplementary Table S1) of various FGT sample, the decrease of T_2 is consistent. The intrinsic coherence time of the NV centers (bare diamond) is approximately 4.5 μs in our diamond chips⁴⁷.

Thus, the decrease of T_2 originates from the magnetic noise generated by critical fluctuations. Further details are provided in Supplementary Section 2.

Spin fluctuation behavior throughout the complete phase transition

In the preceding experiments, the distance d from the FGT layer to the ensemble NV centers layer is about 60 nm⁵⁰ without inserting hBN flakes. As $T \rightarrow T_c$, critical fluctuations intensify dramatically, leading to complete suppression of coherence. The statistical method illustrated in Fig. 3a fails to yield reliable results when T_2 is extremely short, so the critical fluctuations at phase transitions can not be detected. We can mitigate this difficulty by inserting the hBN flakes with finite thickness between the diamond chip and the FGT sample. This configuration increases the distance d , thereby reducing the magnetic noise coupling to the NV centers. This protocol enables us to investigate thickness-dependent decoherence rates of NV centers with an individual FGT sample (see Supplementary Section 7). Preliminary estimation indicates magnetic fluctuations decay scaling as $\langle \delta B^2 \rangle \sim d^{-2.5}$.

Therefore, by increasing the distance d , the measured spin noise decreases, enabling the measurement of the T_2 of NV centers across T_c . Figure 4a shows three decoherence curves at 190 K,

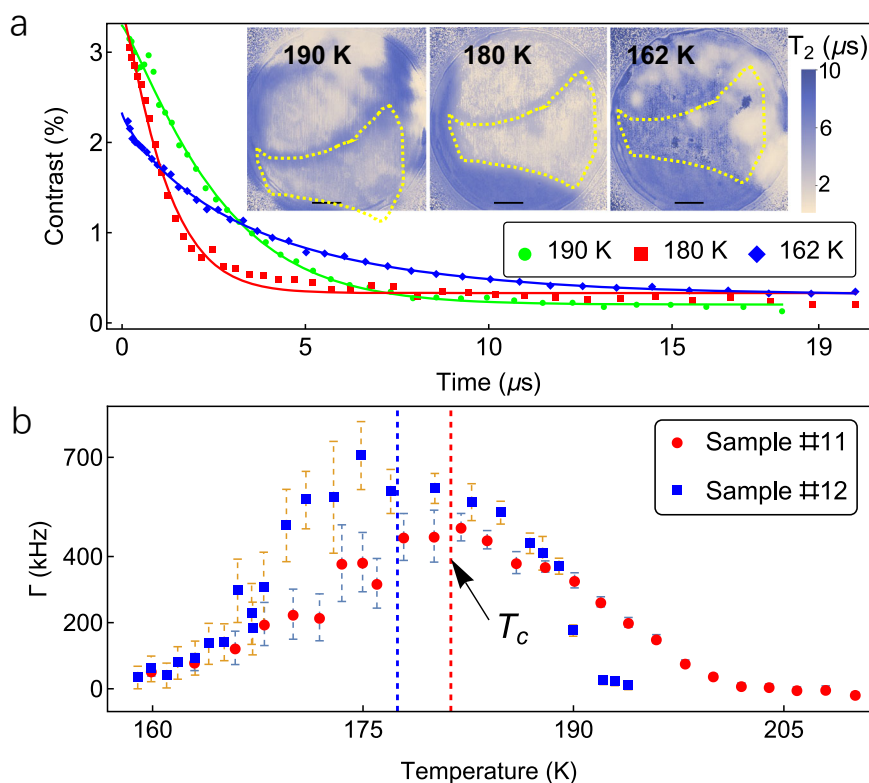


Fig. 4 | Coherence of NV centers across the critical point. **a** Decoherence curves for the entire region delineated by the green dashed line in the inset at three temperatures: above T_c (190 K, green point), near T_c (180 K, red square), and below T_c (162 K, blue rhombus). Solid lines represent fits using Eq. (1), yielding $\alpha = 1.183 \pm 0.055$ (green), 1.187 ± 0.098 (red), 0.845 ± 0.028 (blue). The inset shows the T_2 map measured from Sample #12 at these three temperatures. **b** Decoherence

rate Γ of NV centers as a function of temperature across T_c . Data are shown for two samples with distinct thicknesses and distances d : Sample #11 (47 nm thickness, $d = 310$ nm) and Sample #12 (16 nm thickness, $d = 245$ nm). Vertical dashed lines indicate the T_c determined from the maximum. Error bars represent the standard error of Γ for pixels within the dashed boundaries of Supplementary Figs. S8 and S9. Scale bar: 5 μm .

180 K, and 162 K, corresponding to temperatures above, near, and below T_c . Obviously, the shortest T_2 occurs at 180 K, closest to T_c . In the ferromagnetic state ($T < T_c$), significant magnetic noise variations emerge within the FGT sample, as shown in the inset of Fig. 4a. The data processing strategy illustrated in Fig. 3a becomes inadequate. Instead, we integrate data from all pixels within the region of interest to extract the characteristic coherence time. For $T > T_c$, both data processing methods yield consistent results, as demonstrated in Supplementary Section 8. This consistency confirms the reliability of our experimental data and reflects global properties rather than localized features.

Analogous to the relaxation rate^{39–41}, the decoherence rate is defined as $\Gamma = 1/T_2 - 1/T_{2,0}$, where $T_{2,0}$ denotes the intrinsic coherence time of NV centers in the absence of FGT sample. The decoherence rates of NV centers measured with FGT samples #11 and #12 are presented in Fig. 4b with corresponding T_2 maps provided in Supplementary Figs. S8 and S9. Despite differences in sample thickness and NV-FGT separation distances, the experimental results for both samples exhibit consistent behavior. The decoherence rate is observed to peak at the critical point, coinciding with the strongest fluctuations. This finding aligns with theoretical predictions from ref. 15. Remarkably, even at NV-FGT separations of hundreds of nanometers, magnetic fluctuations in the MHz frequency range exhibit intensities of hundreds of kHz—far exceeding those reported in prior relaxation-based measurements. This contrast in noise intensity between MHz and GHz frequencies directly reflects the spectral structure of critical fluctuations.

Theoretical model based on scaling theory

Building on these observations, we can now elucidate the mechanisms underlying experimental results. The two questions posed in the Introduction can be resolved. The effective Hamiltonian of the NV centers should be written as¹⁸

$$H = \Delta_0 \left(\hat{S}_z^2 - \frac{1}{3} \right) + \gamma (B_0 + \delta B) \hat{S}_z, \quad (2)$$

where $\Delta_0 = 2.87$ GHz is the zero-field splitting level, \hat{S}_z is the Pauli operator, B_0 is the bias field, and δB is the fluctuation field generated by FGT flakes. The coefficient $\gamma = 28$ MHz mT⁻¹ is the electron gyromagnetic ratio. This noise δB induces a decoherence process determined by $\langle \exp(i\phi(t)) \rangle = \exp(-\langle \phi(t)^2 \rangle / 2)$, where $\phi(t) = \gamma \int_0^t \delta B(t') dt'$ is the accumulated phase. According to the fluctuation-dissipation theorem^{51,52}, $\langle \delta B(t_1) \delta B(t_2) \rangle = \frac{1}{2\pi} \int d\omega \exp(-i\omega(t_1 - t_2)) S(\omega)$, where $S(\omega)$ is the power spectral density. Then we have (see Eq. (1))

$$\chi(t) \sim \frac{1}{2} \langle \phi^2(t) \rangle = \frac{1}{4\pi} \int d\omega S(\omega) W_t(\omega), \quad (3)$$

with a frequency filter function for the Hahn-echo pulse sequence by $W_t(\omega) = 8 \sin(\omega t/4)^4 / \omega^2$ ⁴⁶. Thus for noise with the $S(\omega) \sim 1/\omega^\mu$, we have

$$\chi(t) \sim \int d\omega \frac{\sin(\omega t/4)^4}{\omega^2} \frac{1}{\omega^\mu} \sim t^{1+\mu}. \quad (4)$$

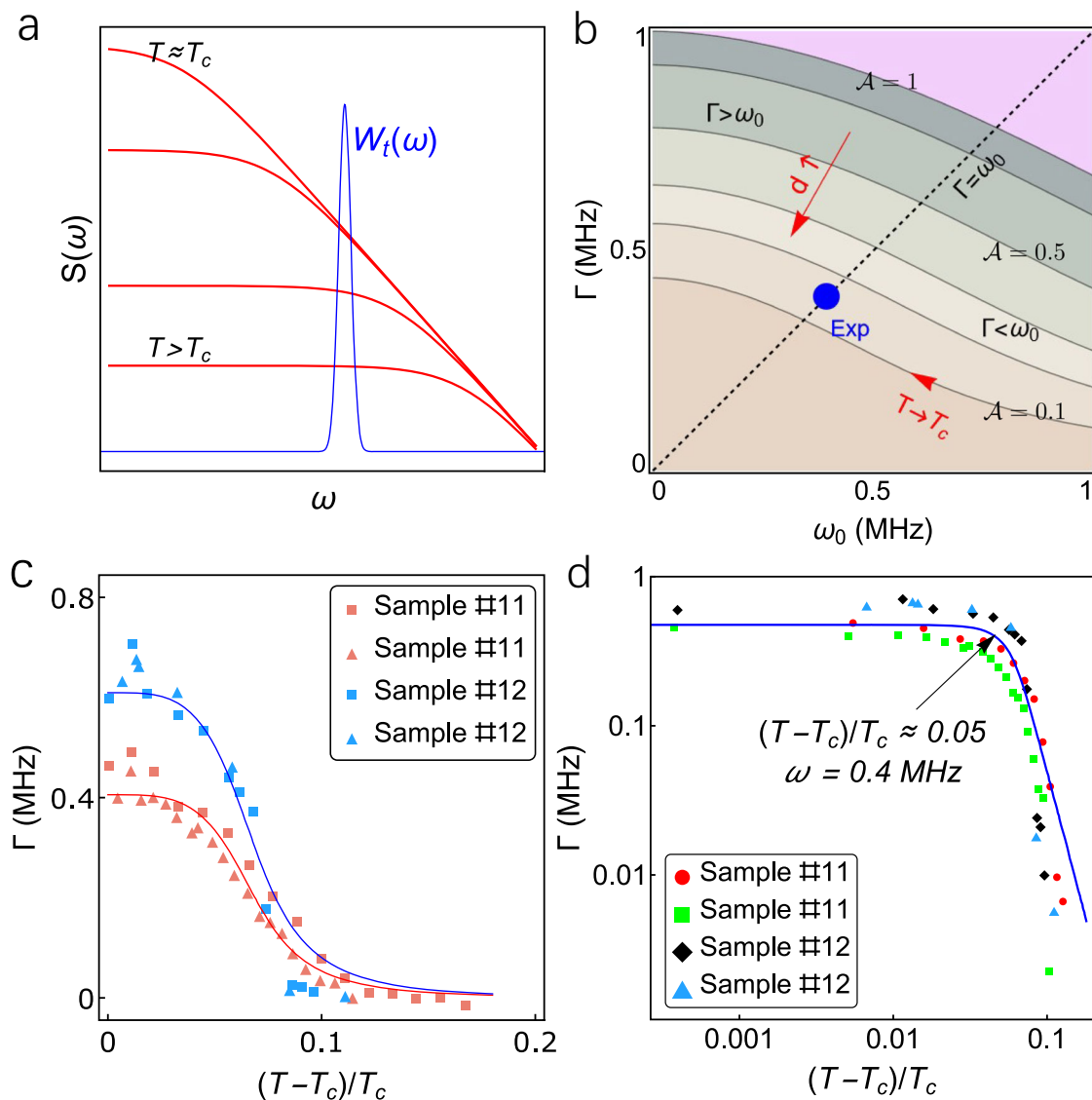


Fig. 5 | Theoretical interpretation of enhanced decoherence rates via noise spectral analysis. **a** Red lines: temperature-dependent magnetic noise spectral density $S(\omega)$ of spin fluctuations; blue line: filter function $W_t(\omega)$ of the Hahn-echo pulse sequence. **b** Contour maps of parameter \mathcal{A} versus Γ and ω_0 for $\mathcal{A} = 0.1, 0.5$, and 1 . Red arrows denote parameter evolution driven by increasing distance d and

approaching T_c , respectively. The blue point corresponds to the experimental results, and the black dashed line marks the condition $\Gamma = \omega_0$, dividing the parameter space into two regimes: $\Gamma > \omega_0$ and $\Gamma < \omega_0$. **c** Fitted Γ (see Eq. (6)) versus $(T - T_c)/T_c$ measured from multiple samples. **d** Double-logarithmic representation of (c); Arrow marks the crossover from white-noise plateau to $1/f$ -slope region.

Inspired by the numerical results from Monte Carlo simulations in ref. 15,17, we hypothesize that the magnetic noise spectrum of critical fluctuations can be approximated by

$$S(\omega) = A/(\omega_0^\mu + \omega^\mu), \quad (5)$$

where $\omega_0 \sim |(T - T_c)/T_c|^{2\nu}$ is the reciprocal of the relaxation time⁵³, an intrinsic property of the sample. z is the dynamic critical exponent associated with the relaxation time, and ν is the critical exponent associated with the divergence of the correlation length. As shown in Fig. 5a, this formula matches the characteristics across both low-frequency and high-frequency asymptotic regimes perfectly. The characteristic frequency ω_0 marks the crossover between white noise and $1/f$ noise regimes. This noise spectrum is dominated by white noise for $\omega \ll \omega_0$, whereas it exhibits $1/f$ -type scaling when $\omega \gg \omega_0$.

In the following, we bridge the experimental results with theoretical models. As shown in Fig. 5a, the filter function $W_t(\omega)$

peaks at $\omega t \simeq 1$, where t represents the interval of pulse sequences. Only noise components near $\omega \simeq 1/t$ contribute to the decoherence, while other frequency components are filtered out. The noise spectrum $S(\omega)$ can be reconstructed from the decoherence profile of a single NV center^{54–56}. However, the decoherence profile of ensemble NV centers constitutes a superposition of decoherence curves of spatially indistinguishable NV centers, inherently complex and lacking direct physical interpretation⁴⁷. Usually, the stretch exponents α qualitatively reflect spatial inhomogeneity of fluctuation field^{57,58}, consistent with our results (see Supplementary Section 6).

Unlike the stretch exponent α , the decoherence rate Γ is independent of the specific decoherence profiles. When $T_2 \ll T_{2,0}$, Γ can be approximated as $1/T_2$, thereby yields $\chi(1/\Gamma) = 1$. Since $W_t(\omega)$ is narrow compared with $S(\omega)$ in the frequency range, substituting t with $1/\Gamma$ into Eq. (3) yields $1 = S(\Gamma) \int W_{1/\Gamma}(\omega) d\omega = \pi S(\Gamma)/2\Gamma$. This establishes a quantitative correspondence between experimental observations and the

theoretical framework:

$$S(\Gamma) = \frac{\mathcal{A}}{\omega_0^\mu + \Gamma^\mu} = \Gamma, \quad (6)$$

where \mathcal{A} is a distance-dependent parameter determined by the NV-FGT separation d . The interplay between Γ , ω_0 and \mathcal{A} is illustrated in Fig. 5b. For a fixed \mathcal{A} (thus fixed d), the asymptotic behavior $\omega_0 \rightarrow 0$ as $T \rightarrow T_c$ reflects critical slowing down. Moreover, increasing d reduces \mathcal{A} (since $\lim_{d \rightarrow \infty} \mathcal{A} = 0$), thereby reducing Γ . Employing the scaling relation $\omega_0 = m|(T - T_c)/T_c|^{z\nu}$, where m is a fitting parameter, the temperature dependence of Γ is obtained. As shown in Fig. 5c, the experimentally measured Γ values align well with theoretical predictions derived from Eq. (6), where m and \mathcal{A} are determined via global fitting of the data. This analysis adopts critical exponents ($\nu = 1$ and $z = 2.17$, yielding $\mu = 1 + \gamma/z\nu = 1.81$) from the 2D Ising model to describe the magnetism of FGT^{15,22,23,25,26}. Crucially, the developed theoretical framework here is universal, independent to the specific spin Hamiltonian.

There are two intriguing limits,

$$\Gamma \sim \begin{cases} \text{constant} & \omega_0 \ll \Gamma \\ \left| \frac{T - T_c}{T_c} \right|^{-2/\mu} & \omega_0 \gg \Gamma. \end{cases} \quad (7)$$

Both limits and their crossover are distinctly evident in the log–log representation. As illustrated in Fig. 5d, all four independent measurements exhibit nearly identical behavior. The crossover is given by $\Gamma = \omega_0$. Notably, in the vicinity of $(T - T_c)/T_c \approx 0.05$, the relaxation time of critical fluctuations reaches approximately $1/\omega_0 \sim 2.5 \mu\text{s}$. This value represents an intrinsic property of the FGT material and remains independent of experimental configurations. By adjusting the NV-FGT separation distance, additional spin correlation times can be probed at distinct reduced temperatures. To our knowledge, this work constitutes the first experimental determination of spin-correlation times in real physical systems undergoing phase transitions.

Discussion

In summary, this work reports an experimental demonstration that links critical fluctuation phenomena to scaling theory. A noise crossover signature emerges from the temperature-dependent evolution of NV centers' coherence times. Inspired by numerical results, we propose a phenomenological noise spectrum formula that exhibits excellent agreement with measurements. Wide-field magnetic imaging provides robust global properties of the sample but neglects local inhomogeneities. Notably, our research unveils a paradigm for characterizing criticality through microscopic dynamical quantities, advancing systematic methodologies for phase transition analysis. We anticipate that in the future, the correlation time, correlation length, and their corresponding critical exponents will be determined through single NV center-based experiments.

Methods

Extended information on used methods is provided in Supplementary information.

Data availability

The raw data that support the findings of this study are available in FigShare and "Source Data" section. Source data are provided with this paper.

References

- Elliott, R. *Magnetic Phase Transitions* (pp. 2–24. Springer Berlin Heidelberg, Berlin, Heidelberg, 1983).
- Hohenberg, P. C. & Halperin, B. I. Theory of dynamic critical phenomena. *Rev. Mod. Phys.* **49**, 435–479 (1977).

- Sachdev, S. *Quantum Phase Transitions* (Cambridge University Press, Cambridge, 2011), 2 edn.
- Kadanoff, L. P. et al. Static phenomena near critical points: theory and experiment. *Rev. Mod. Phys.* **39**, 395–431 (1967).
- Fisher, M. E. The renormalization group in the theory of critical behavior. *Rev. Mod. Phys.* **46**, 597–616 (1974).
- Wilson, K. G. & Kogut, J. The renormalization group and the ϵ expansion. *Phys. Rep.* **12**, 75–199 (1974).
- Herbut, I. *A Modern Approach to Critical Phenomena*. (Cambridge University Press, Cambridge, 2007).
- Liu, B. et al. Critical behavior of the van der Waals bonded high T_c ferromagnet Fe_3GeTe_2 . *Sci. Rep.* **7**, 6184 (2017).
- Tan, C. et al. Hard magnetic properties in nanoflake van der Waals Fe_3GeTe_2 . *Nat. Commun.* **9**, 1554 (2018).
- Lewinska, S. et al. Magnetic susceptibility and phase transitions in LiNiPO_4 . *Phys. Rev. B* **99**, 214440 (2019).
- Rost, A. W. et al. Power law specific heat divergence in $\text{Sr}_3\text{Ru}_2\text{O}_7$. *Phys. status solidi (b)* **247**, 513–515 (2010).
- Salathé, Y. et al. Digital quantum simulation of spin models with circuit quantum electrodynamics. *Phys. Rev. X* **5**, 021027 (2015).
- Landauer, R. The noise is the signal. *Nature* **392**, 658–659 (1998).
- Machado, F., Demler, E. A., Yao, N. Y. & Chatterjee, S. Quantum noise spectroscopy of dynamical critical phenomena. *Phys. Rev. Lett.* **131**, 070801 (2023).
- Chen, Z. & Yu, C. C. Measurement-noise maximum as a signature of a phase transition. *Phys. Rev. Lett.* **98**, 057204 (2007).
- Kwan-tai, L. Dynamic exponent for 2D Ising model by power spectra method. *J. Phys. A: Math. Gen.* **26**, 6691 (1993).
- Chen, Z. & Yu, C. C. Noise spectra of stochastic pulse sequences: application to large-scale magnetization flips in the finite size two-dimensional Ising model. *Phys. Rev. B* **79**, 144420 (2009).
- Schirhagl, R., Chang, K., Lorez, M. & Degen, C. L. Nitrogen-vacancy centers in diamond: nanoscale sensors for physics and biology. *Annu. Rev. Phys. Chem.* **65**, 83–105 (2014).
- Doherty, M. W. et al. The nitrogen-vacancy colour centre in diamond. *Phys. Rep.* **528**, 1–45 (2013).
- Du, J., Shi, F., Kong, X., Jelezko, F. & Wrachtrup, J. Single-molecule scale magnetic resonance spectroscopy using quantum diamond sensors. *Rev. Mod. Phys.* **96**, 025001 (2024).
- Deiseroth, H. J., Aleksandrov, K., Reiner, C., Kienle, L. & Kremer, R. K. Fe_3GeTe_2 and Ni_3GeTe_2 -two new layered transition metal compounds: crystal structures, HRTEM investigations, and magnetic and electrical properties. *Eur. J. Inorg. Chem.* **2006**, 1561–1567 (2006).
- Fei, Z. et al. Two-dimensional itinerant ferromagnetism in atomically thin Fe_3GeTe_2 . *Nat. Mater.* **17**, 778–782 (2018).
- Deng, Y. et al. Gate-tunable room-temperature ferromagnetism in two-dimensional Fe_3GeTe_2 . *Nature* **563**, 94–99 (2018).
- Zhang, R. & Willis, R. F. Thickness-dependent Curie temperatures of ultrathin magnetic films: Effect of the range of spin-spin interactions. *Phys. Rev. Lett.* **86**, 2665–2668 (2001).
- Zhao, M. et al. Kondo holes in the two-dimensional itinerant Ising ferromagnet Fe_3GeTe_2 . *Nano Lett.* **21**, 6117–6123 (2021).
- Liu, J. et al. Insight into magnetic characteristics of an Ising monolayer Fe_3GeTe_2 structure. *Micro Nanostruct.* **177**, 207549 (2023).
- Scholten, S. C. et al. Widefield quantum microscopy with nitrogen-vacancy centers in diamond: strengths, limitations, and prospects. *J. Appl. Phys.* **130**, 150902 (2021).
- Casola, F., van der Sar, T. & Yacoby, A. Probing condensed matter physics with magnetometry based on nitrogen-vacancy centres in diamond. *Nat. Rev. Mater.* **3**, 17088 (2018).
- Gross, I. et al. Real-space imaging of non-collinear anti-ferromagnetic order with a single-spin magnetometer. *Nature* **549**, 252–256 (2017).

30. Song, T. et al. Direct visualization of magnetic domains and moiré magnetism in twisted 2D magnets. *Science* **374**, 1140–1144 (2021).
31. Bhattacharyya, P. et al. Imaging the Meissner effect in hydride superconductors using quantum sensors. *Nature* **627**, 73–79 (2024).
32. Balasubramanian, G. et al. Nanoscale imaging magnetometry with diamond spins under ambient conditions. *Nature* **455**, 648–651 (2008).
33. Suter, D. & Álvarez, G. A. Colloquium: protecting quantum information against environmental noise. *Rev. Mod. Phys.* **88**, 041001 (2016).
34. de Lange, G., Wang, Z. H., Risté, D., Dobrovitski, V. V. & Hanson, R. Universal dynamical decoupling of a single solid-state spin from a spin bath. *Science* **330**, 60–63 (2010).
35. Du, J. et al. Preserving electron spin coherence in solids by optimal dynamical decoupling. *Nature* **461**, 1265–1268 (2009).
36. Wang, Z.-H., de Lange, G., Risté, R., Hanson, D. & Dobrovitski, V. Comparison of dynamical decoupling protocols for a nitrogen-vacancy center in diamond. *Phys. Rev. B* **85**, 155204 (2012).
37. Wang, Y.-X. et al. Visualization of bulk and edge photocurrent flow in anisotropic Weyl semimetals. *Nat. Phys.* **19**, 507–514 (2023).
38. Vezvae, A., Shitara, N., Sun, S. & Montoya-Castillo, A. Fourier transform noise spectroscopy. *npj Quantum Inf.* **10**, 52 (2024).
39. Huang, M. et al. Wide field imaging of van der Waals ferromagnet Fe₃GeTe₂ by spin defects in hexagonal boron nitride. *Nat. Commun.* **13**, 5369 (2022).
40. McLaughlin, N. J. et al. Quantum imaging of magnetic phase transitions and spin fluctuations in intrinsic magnetic topological nanoflakes. *Nano Lett.* **22**, 5810–5817 (2022).
41. Huang, M. et al. Layer-dependent magnetism and spin fluctuations in atomically thin van der Waals magnet CrPS₄. *Nano Lett.* **23**, 8099–8105 (2023).
42. Ziffer, M. E. et al. Quantum noise spectroscopy of criticality in an atomically thin magnet. Preprint at *arXiv* <https://arxiv.org/abs/2407.05614> (2024).
43. Huang, M. et al. Revealing intrinsic domains and fluctuations of moiré magnetism by a wide-field quantum microscope. *Nat. Commun.* **14**, 5259 (2023).
44. Wang, C. et al. Thermal-activated escape of the bistable magnetic states in 2D Fe₃GeTe₂ near the critical point. *Commun. Phys.* **6**, 351 (2023).
45. Zhang, X.-Y. et al. ac susceptometry of 2D van der Waals magnets enabled by the coherent control of quantum sensors. *PRX Quantum* **2**, 030352 (2021).
46. Degen, C. L., Reinhard, F. & Cappellaro, P. Quantum sensing. *Rev. Mod. Phys.* **89**, 035002 (2017).
47. Bauch, E. et al. Decoherence of ensembles of nitrogen-vacancy centers in diamond. *Phys. Rev. B* **102**, 134210 (2020).
48. Dobrovitski, V. V., Feiguin, A. E., Awschalom, D. D. & Hanson, R. Decoherence dynamics of a single spin versus spin ensemble. *Phys. Rev. B* **77**, 245212 (2008).
49. Park, H., Lee, J., Han, S., Oh, S. & Seo, H. Decoherence of nitrogen-vacancy spin ensembles in a nitrogen electron-nuclear spin bath in diamond. *npj Quantum Inf.* **8**, 95 (2022).
50. Ziegler, J. F., Ziegler, M. & Biersack, J. Srim - the stopping and range of ions in matter (2010). *Nucl. Instrum. Methods Phys. Res. Sect. B* **268**, 1818–1823 (2010).
51. Ryogo Kubo, N. H., Morikazu Toda. *Statistical Physics II: Nonequilibrium Statistical Mechanics*. Chapter 4, pp 146–202 (Springer, Berlin, Heidelberg, 1991), 2nd edn.
52. Kubo, R. The fluctuation-dissipation theorem. *Rep. Prog. Phys.* **29**, 255 (1966).
53. Bhatt, R. N. & Young, A. P. A new method for studying the dynamics of spin glasses. *Europhys. Lett.* **20**, 59 (1992).
54. Álvarez, G. A. & Suter, D. Measuring the spectrum of colored noise by dynamical decoupling. *Phys. Rev. Lett.* **107**, 230501 (2011).
55. Yuge, T., Sasaki, S. & Hirayama, Y. Measurement of the noise spectrum using a multiple-pulse sequence. *Phys. Rev. Lett.* **107**, 170504 (2011).
56. Krzywda, J., Szankowski, P. & Cywinski, L. The dynamical-decoupling-based spatiotemporal noise spectroscopy. *N. J. Phys.* **21**, 043034 (2019).
57. Ediger, M. D. Spatially heterogeneous dynamics in supercooled liquids. *Annu. Rev. Phys. Chem.* **51**, 99–128 (2000).
58. Gezo, J. et al. Stretched exponential spin relaxation in organic superconductors. *Phys. Rev. B* **88**, 140504 (2013).
59. Fe₃GeTe₂ crystal structure: Datasheet from “Pauling file multinationals edition—2022” in *springermaterials*. https://materials.springer.com/isp/crystallographic/docs/sd_1608618.

Acknowledgements

This work was supported by the National Natural Science Foundation of China (grant No. T2125011 (F.S.), U23A2074 (M.G.)), the CAS Project for Young Scientists in Basic Research (grant No. YSBR-O68 (F.S.), YSBR-O49 (H.Z.)), Innovation Program for Quantum Science and Technology (Grant No. 2021ZD0302200 (J.D.), 2021ZD0303204 (F.S.), 2021ZD0301200 (M.G.), 2021ZD0301500 (M.G.), 2021ZD0302800 (H.Z.)), the National Key Research and Development Program of China (Grant No. 2023YFB4502500 (F.S.)), the Strategic Priority Research Program of the Chinese Academy of Sciences (Grant No. XDB0500000 (M.G.)), New Cornerstone Science Foundation through the XPLOER PRIZE (F.S.), Postdoctoral Fellowship Program of CPSF (Grant No. GZC20232558 (Z.D.)) and the Fundamental Research Funds for the Central Universities (F.S. and H.Z.). This work was partially carried out at the USTC Center for Micro- and Nanoscale Research and Fabrication and the Instruments Center for Physical Science, University of Science and Technology of China.

Author contributions

F.S., J.D., M.G., H.Z., and Z.D. supervised and directed this work. F.S., H.Z., M.G. and Y.L. conceived the original experiment idea. Y.L., Z.C. and P.W. built the experiment setup. Y.L. and Z.D. conducted the experiments and analyzed data. C.W. and H.Z. provided and fabricated the FGT sample. H.S. and Y.W. provided the diamond chips with NV centers. M.G. and Y.L. developed the theory frameworks. Y.L., M.G., Z.D., H.Z. and F.S. wrote and further revised the paper. All the authors commented on the paper and approved the submission.

Competing interests

The authors declare no competing interests.

Additional information

Supplementary information The online version contains supplementary material available at <https://doi.org/10.1038/s41467-025-63578-w>.

Correspondence and requests for materials should be addressed to Ming Gong, Hualing Zeng or Fazhan Shi.

Peer review information *Nature Communications* thanks the anonymous reviewers for their contribution to the peer review of this work. A peer review file is available.

Reprints and permissions information is available at <http://www.nature.com/reprints>

Publisher's note Springer Nature remains neutral with regard to jurisdictional claims in published maps and institutional affiliations.

Open Access This article is licensed under a Creative Commons Attribution-NonCommercial-NoDerivatives 4.0 International License, which permits any non-commercial use, sharing, distribution and reproduction in any medium or format, as long as you give appropriate credit to the original author(s) and the source, provide a link to the Creative Commons licence, and indicate if you modified the licensed material. You do not have permission under this licence to share adapted material derived from this article or parts of it. The images or other third party material in this article are included in the article's Creative Commons licence, unless indicated otherwise in a credit line to the material. If material is not included in the article's Creative Commons licence and your intended use is not permitted by statutory regulation or exceeds the permitted use, you will need to obtain permission directly from the copyright holder. To view a copy of this licence, visit <http://creativecommons.org/licenses/by-nc-nd/4.0/>.

© The Author(s) 2025